Available online at www.sciencedirect.com
ScienceDirect
Icarus 191 (2007) 211–222
ICARUS
www.elsevier.com/locate/icarus

Titan's surface from Cassini RADAR SAR and high resolution radiometry data of the first five flybys

F. Paganelli [a,*], M.A. Janssen [a], B. Stiles [a], R. West [a], R.D. Lorenz [b], J.I. Lunine [c,d], S.D. Wall [a], P. Callahan [a], R.M. Lopes [a], E. Stofan [e], R.L. Kirk [f], W.T.K. Johnson [a], L. Roth [a], C. Elachi [a], the Radar Team

[a] *Jet Propulsion Laboratory, California Institute of Technology, 4800 Oak Grove Dr., Pasadena, CA 91109, USA*
[b] *Space Department, Planetary Exploration Group, Johns Hopkins University Applied Physics Lab, 11100 Johns Hopkins Road, Laurel, MD 20723-6099, USA*
[c] *Lunar and Planetary Laboratory, University of Arizona, Tucson, AZ 85721, USA*
[d] *IFSI, INAF, Rome 00133, Italy*
[e] *Proxemy Research, Bowie, MD 20715, USA*
[f] *US Geological Survey, Flagstaff, AZ 86001, USA*

Received 17 October 2006; revised 9 April 2007

Available online 24 May 2007

Abstract

The first five Titan flybys with Cassini's Synthetic Aperture RADAR (SAR) and radiometer are examined with emphasis on the calibration and interpretation of the high-resolution radiometry data acquired during the SAR mode (SAR-radiometry). Maps of the 2-cm wavelength brightness temperature are obtained coincident with the SAR swath imaging, with spatial resolution approaching 6 km. A preliminary calibration shows that brightness temperature in these maps varies from 64 to 89 K. Surface features and physical properties derived from the SAR-radiometry maps and SAR imaging are strongly correlated; in general, we find that surface features with high radar reflectivity are associated with radiometrically cold regions, while surface features with low radar reflectivity correlate with radiometrically warm regions. We examined scatterplots of the normalized radar cross-section σ^0 versus brightness temperature, finding differing signatures that characterize various terrains and surface features. Implications for the physical and compositional properties of these features are discussed. The results indicate that volume scattering is important in many areas of Titan's surface, particularly Xanadu, while other areas exhibit complex brightness temperature variations consistent with variable slopes or surface material and compositional properties.

Keywords: Titan; Radar observations; Satellites, surfaces; Saturn, satellites

1. Introduction

Synthetic Aperture Radar (SAR) and passive microwave radiometry are two of the operational modes of the K_u-band (13.78 GHz, $\lambda = 2.18$ cm) Cassini Titan Radar Mapper (Elachi et al., 2005a). The radiometry data presented in this paper were acquired during the SAR active mode, which cycles among five antenna beams orthogonal to the subspacecraft track on Titan. These data are unique as they are temporally and spatially co-registered with SAR imaging, therefore allowing a direct comparison of surface features based on their correlated radiometric and scattering properties. This correlation is limited in spatial resolution by the radiometry footprint at closest approach, precluding detection and correlation of surface features smaller than 6-km resolution. Antenna sidelobe contributions and a variable calibration among the five radiometer beams caused by sidelobes must be taken into account to obtain accurate relative brightness variations.

In this paper we outline the radiometric calibration process and discuss the significance of the resulting high-resolution radiometry maps, in context with the radar reflectivity, for understanding Titan's geological and physical properties. We will refer to the high-resolution radiometric maps as SAR-radiometry

* Corresponding author.
E-mail address: flora.paganelli@jpl.nasa.gov (F. Paganelli).

0019-1035/$ – see front matter
doi:10.1016/j.icarus.2007.04.032

Table 1
Nominal radiometer characteristics

Frequency	13.78 GHz
Wavelength	2.18 cm
Bandwidth	135 MHz
Measurement noise	0.025 K/Hz
Beamwidth (Beam 3)	0.35° × 0.35°
Beamwidths (Beam 1, 2, 4, 5)	0.35° (along track) × 1.35° (across track)
Footprint width, Beam 3	6 km periapsis, 20 km start/end of SAR
Footprint diameter, Beam 1, 2, 4, 5, cross-track	23 km periapsis, 75 km start/end of SAR

maps, and concentrate on the data obtained in the first five flybys with SAR passes: Ta, T3, T7, T8, and T13. We explore the characterization of surface features seen by the radar in these passes using the correlation of radar reflectivity with radiometric brightness.

2. Radiometry with the Cassini RADAR instrument

The Cassini RADAR instrument includes a passive radiometer mode that operates interleaved with all other modes of the instrument including the SAR mode. Elachi et al. (2005a) describe the objectives, design, and operational characteristics of this instrument including those of the radiometer, the relevant characteristics of which are given in Table 1. The radiometer shares the five-beam feed system of the RADAR that illuminates the 4-m Cassini communications antenna, and measures the radiant power that is collected by this antenna and fed to the RADAR receiver. The central beam ("beam 3") is circularly symmetric, of high gain, with 0.35° half-power beamwidth, while the remaining beams are highly elliptical, of lower gain, with major axes spaced by ∼1° in the cross-track dimension to give maximum dimension to the SAR swath. The radiometer observes the thermal emission from Titan simultaneously with the SAR. Because it measures incoherent thermal radiation, its resolution is limited to the actual beam footprints on the surface. The gain patterns for all beams were accurately measured by scanning the Sun. The pattern determined for beam 3 is shown in Fig. 1. The footprint for beam 3 is as small as 6 km at closest approach (range to Titan center ∼4000 km) enlarging to 20 km at the start or end of the SAR pass (range ∼8000 km). Beam 1, 2, 4, and 5 footprints are correspondently larger.

The radiometer measures the noise power in the radiometer input bandwidth. This power is amplified, converted to a linear voltage output and averaged over discrete time intervals (integration times) to produce digital counts. In the SAR mode these integrations are synchronized with the radar burst cycle, the duration of which typically varies from 130 to 270 ms depending on the distance to the surface of Titan. Each burst cycle includes radiometer integrations on the antenna input (typically two to five integrations of 35 ms each depending on the burst period) and on an internal reference load (one integration of 25 ms). In the long-wavelength (Rayleigh–Jeans) limit of the spectrum, the radiant noise power from a thermal source is linear with blackbody temperature, and is typically measured

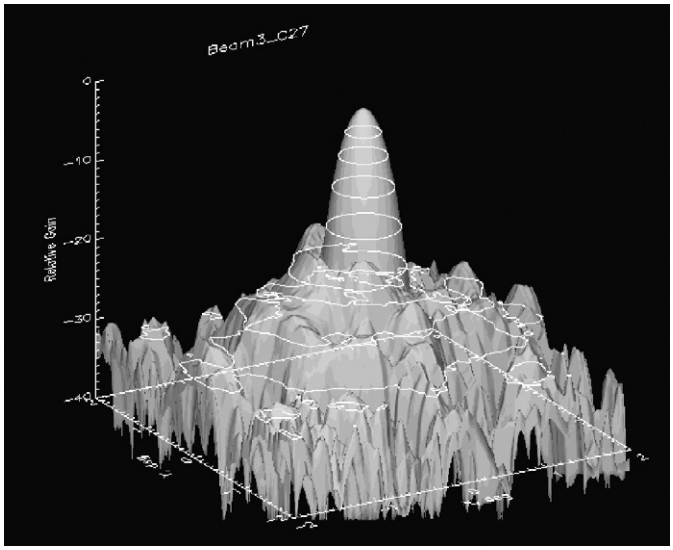

Fig. 1. Beam 3 obtained from the Sun scan after correction for the finite size of the Sun and a best fit of a beam shape model to the main beam. Contour levels are shown at 3, 6, 10, 15, 20 25, and 30 dB below the central peak.

in units of degrees Kelvin. The calibration to obtain brightness in Kelvin units is ultimately accomplished with reference to known sources or thermal targets (cf. Janssen, 1993). The one-sigma noise level of the radiometer is 0.026 K for a 1 s integration time over the 125 MHz bandwidth; consequently, the noise along the SAR track varies from 0.06 to 0.1 K per measurement. Gain is monitored by observing a reference load, the emission from which has been determined empirically to track the overall system gain to about 1%. The zero level of the Kelvin scale is determined by observing cold sky (where $T_b = 2.7$ K) before and/or after the Titan observations. Calibration of the Cassini radiometer is described in a separate paper (Janssen et al., in preparation), and brightness temperatures reported here are based on initial results from this effort (Appendix A). Our emphasis in the present paper is on local variations and correlation with geological terrain types identified in the SAR data. While relative accuracy is important, the absolute calibration is not critical for this purpose. We conservatively estimate the error in all such corrected SAR radiometry tracks to consist of an overall bias of about 5 K, with additional random errors of ∼2 K on scales of 500+ km decreasing to 0.1 K on scales approaching the along-track footprint. Ongoing efforts with present data and the inclusion of more calibrated low-resolution data will reduce these uncertainties.

3. Titan's features seen by SAR and SAR-radiometry

In this section we present and compare the full swaths of SAR and SAR-radiometry obtained from the Ta (October 2004) through the T13 (May 2006) flybys. The SAR maps from these flybys are shown in Fig. 2a and the corresponding SAR-radiometry maps in Fig. 2b. The characteristics of these swaths are listed in Table 2. The SAR swaths show the normalized radar cross section (σ^0) as derived from unprojected, noise-subtracted SAR data without incidence angle correction (Stiles et al., 2006). The SAR-radiometry maps in total show bright-

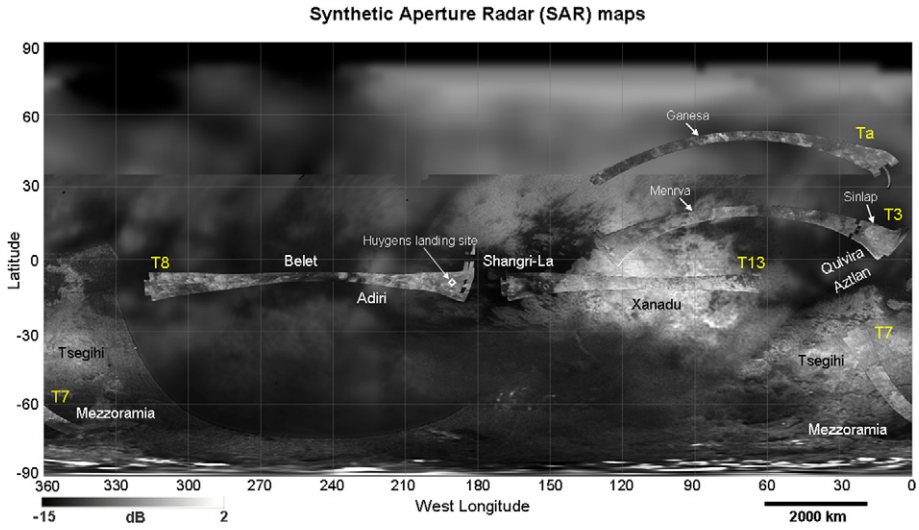

(a)

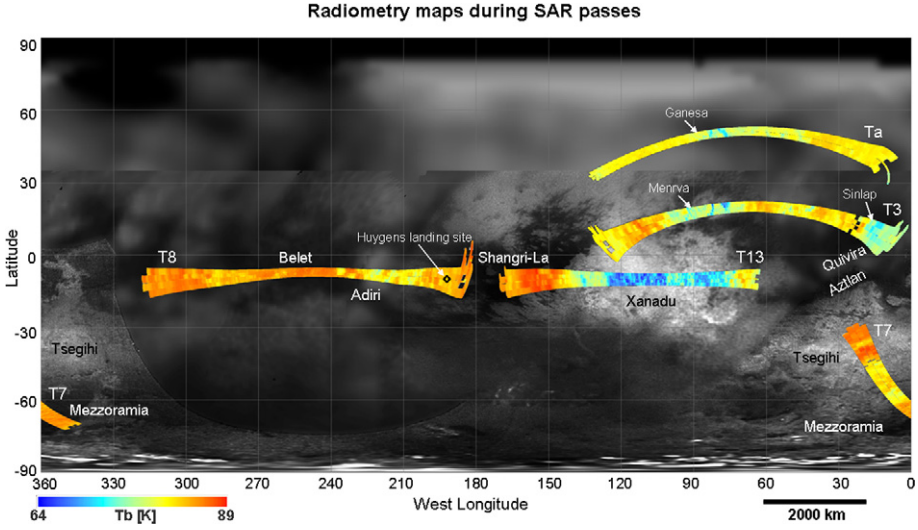

(b)

Fig. 2. (a) Titan map showing SAR swaths of radar cross-section σ^0 for Ta, T3, T7, T8, and T13. The values for σ^0 are noise-subtracted and uncorrected for incidence angle. The swaths are superposed on ISS (1 μm) and Hubble Space Telescope (1 μm) base maps. (b) Titan map showing the Ta, T3, T7, T8 and T13 SAR-radiometry swaths. The swaths are superposed on the same background as (a) and show corresponding calibrated brightness temperatures.

Table 2
Swath characteristics

	Resolution range [km]	Acquisition date	Swath length [km]	Latitude range [°]	Longitude range [°]	Incidence angle [°]
Ta	0.3–1.7	26-10-04	4500	32–53 N	10–130 W	2–46
T3	0.3–1.5	15-02-05	6236	2 S–22.5 N	0.4–133 W	1–30
T7	0.3–1.7	07-9-05	1970	25–75.5 S	0–31/329–360 W	7–35
T8	0.3–1.7	27-10-05	5000	18.5 S–7 N	179–320 W	1–31
T13	0.3–1.5	01-05-06	4000	3 S–18 S	60–172 W	10–29

ness temperatures that vary between the extremes of 64 and 89 K (Table 3).

Unlike with the SAR data, the SAR radiometry data are corrected for incidence angle using a dielectric model to adjust all brightness temperatures to the expected brightness at normal incidence (Janssen et al., in preparation). The individual maps in Fig. 2b have been scaled to a common 64–89 K range to show relative variability and enable cross-comparison. To provide a context, the SAR and SAR-radiometry maps are overlain on Titan's ISS near-IR (1 μm) coverage (Porco et al., 2005), and in the high northern latitudes, where ISS imaging is not available, on Hubble Space Telescope (HST) near-IR (1 μm) coverage (Smith et al., 1996). Figs. 3–7 show detailed comparisons for each swath: Ta, T3, T7, T8 and T13. Each figure shows the SAR map in the same gray scale as Fig. 2a, now overlain with the SAR radiometry using the same color scale as Fig. 2b.

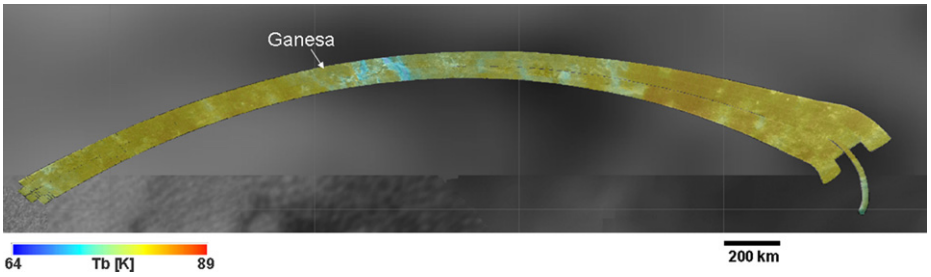

Fig. 3. Integrated SAR and SAR-radiometry swath for Ta. North to the top.

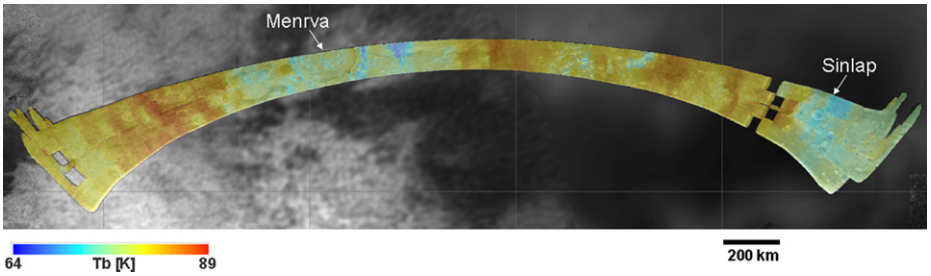

Fig. 4. Integrated SAR and SAR-radiometry swath for T3. North to the top.

Table 3
Swath brightness temperature T_b [K]

Swath	T_b min	T_b max	T_b avg.
Ta	69.47	83.61	80.19
T3	65.33	87.34	79.74
T7	76.47	88.20	83.66
T8	74.15	87.55	83.85
T13	63.99	88.69	77.89

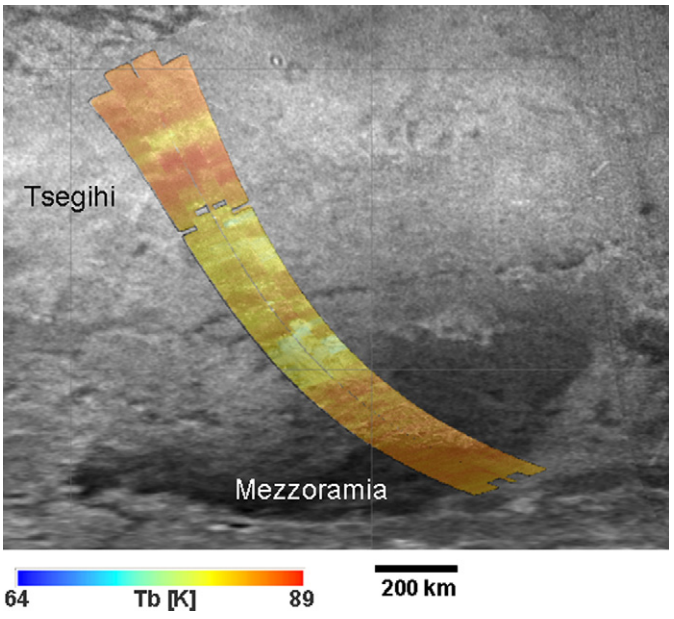

Fig. 5. Integrated SAR and SAR-radiometry swath for T7. North to the top.

Correlations are readily apparent between SAR and SAR-radiometry maps, and with ISS maps where available. Generally we see regions with high radar reflection showing low brightness temperatures, while features with low radar reflection exhibit high brightness temperatures. To enable a quantitative comparison between the SAR radiometry and the much higher resolution SAR data, both data sets were averaged to a common 20-km grid that approximates an average resolution for the radiometry. The reduction procedure for the SAR data consisted of the application of a low-pass filter and rescaling to obtain a 20-km cell resolution grid. The same process was used to place the calibrated brightness temperature swaths on the same grid. The matching σ^0 and radiometry data on this grid were then examined collectively using local and global scatterplots. The correlation of radar reflection and brightness temperature for all the swaths is shown in the cumulative scatterplot of Fig. 8. The general trend of the correlation noted above is evident, with clusters indicating differing behaviors that may characterize various terrains and geologic features. Detailed comparisons and geophysical considerations are given in the following section, while we conclude here with a discussion of possible physical causes for the observed brightness temperature variations.

The principal cause of these variations is expected to be variation in emissivity. The topography seen so far on Titan is only of the order of a few hundred meters, and taking into account the near-surface vertical temperature lapse rate on Titan, topography can only account for brightness temperature variations of typically 1 K or less (Lorenz et al., 2003). This suggests that physical temperature variations are likely very small across the swaths and brightness temperature (T_b) variations can be ascribed to variations in emissivity (e) as

$$T_b = e^* T_{\text{kin}},$$

where $T_{\text{kin}} = 94$ K. The Huygens probe in situ measurement of Titan surface was of 93.6 K (Fulchignoni et al., 2005). A T_{kin} gradient is expected from equator to pole, and further modeling (outside the scope of this paper) integrating low latitude data with newly acquired and planned data at higher latitude

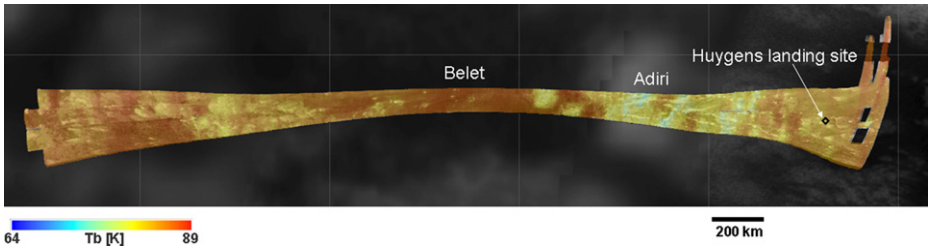

Fig. 6. Integrated SAR and SAR-radiometry swath for T8. North to the top.

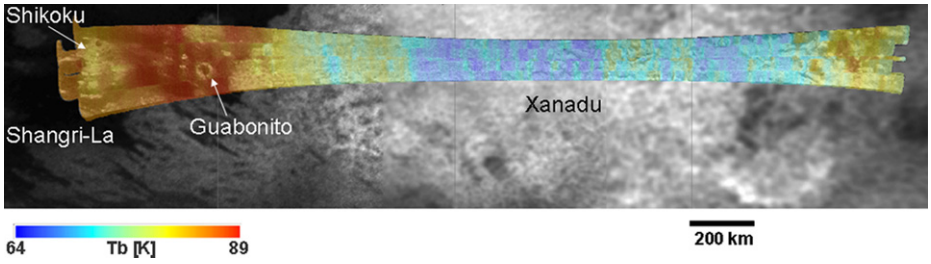

Fig. 7. Integrated SAR and SAR-radiometry swath for T13. North to the top.

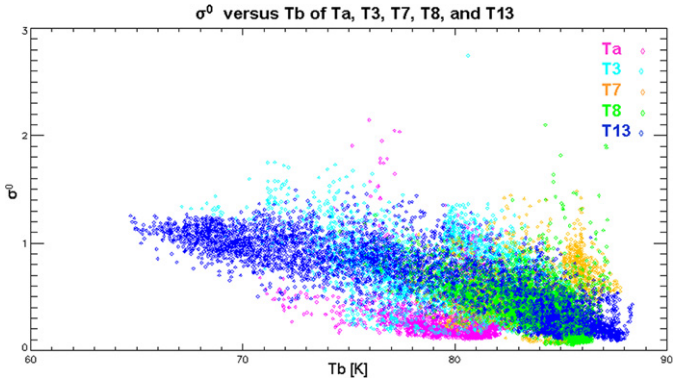

Fig. 8. Cumulative scatterplot of normalized radar cross section (σ^0) versus brightness temperature (T_b) for Ta, T3, T7, T8, T13 swaths showing the correlation between radar reflectivity and brightness temperature.

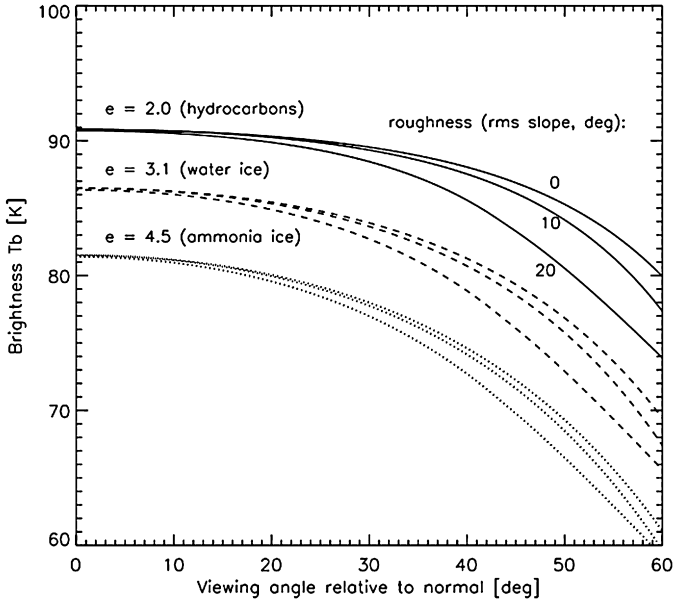

Fig. 9. Values for brightness temperature T_b versus incidence angle for various dielectric constant with rms surface slope between 0 and 20° computed for a simple model for a uniform dielectric surface with roughness on scales greater than the wavelength. The polarization is perpendicular to the plane of incidence consistent with the SAR radiometry. Note that the dependence of roughness on incidence angle effect is most prominent for incidence angles greater than 20°.

(>75 N) would be needed to correctly estimate the global emissivity variation of Titan's surface.

The emissivity of a surface is determined by its chemical and physical properties. To interpret the present data we begin with a simple model for emissivity that is amenable to quantitative analyses and follow by outlining more complex possibilities that will ultimately be needed for a full description. Fig. 9 shows the brightness temperature computed for a uniform dielectric surface at a temperature of 94 K. The emissivity is readily obtained from the Fresnel reflection coefficients for a dielectric half space, using Kirchoff's law for the relation between reflectivity and emissivity (Ulaby et al., 1981; Greffet and Nieto-Vesperinas, 1998). Fig. 9 assumes that the observed polarization is perpendicular to the plane of incidence, which is very close to the case for all the SAR observations.

Surface roughness on scales much larger than the wavelength is included by considering emission from facets distributed with a rms deviation of local normal from vertical shown on the plot as rms slope (White and Cogdell, 1973). The model behavior is shown for materials expected on the surface of Titan; i.e., materials characterized either by solid hydrocarbons (dielectric constant $\varepsilon = 2.0$–2.4; Thompson and Squyers, 1990), water ice ($\varepsilon = 3.1$; Thompson and Squyers, 1990), water–ammonia ice ($\varepsilon = 4.5$; Thompson and Squyers, 1990; Lorenz, 1998), or combinations thereof. Methane can be trapped in ice-like solid called clathrate hydrate. The dielectric constant of clathrates is determined by the proportion of ice/methane molecules in the clathrate hydrate structure and could reach about 1.8 (Hobbs, 1974), slightly lower than solid hydrocarbons or ice alone, thus suggesting the possible pres-

ence of clathrates on Titan surface. Most recent work on the thermal evolution of Titan by Tobie et al. (2006) has suggested the presence of clathrate hydrate within Titan's crust, possibly close to the surface.

The present SAR radiometry data sets have maximum incidence angle excursions up to 30°, the only exception being that of Ta in which the incidence angle is 46° at the beginning of the swath. The simple model of Fig. 9 suggests that we should expect little to no influence from regionally varying rms slope surfaces, and that the predominant cause of the brightness temperature variation is spatial variability of dielectric constant. This is clearly untenable as a general explanation because the great extent of the surface with brightness temperature less than 80 K would have to be explained by a dielectric constant >4.5, requiring bulk constituents not expected to occur in quantity on Titan's surface such as silicate rocks ($\varepsilon = 6$–$9+$; Thompson and Squyers, 1990). A more likely explanation for the lower brightness temperatures is the presence of volume scattering. Volume scattering occurs when the wave that enters the surface is scattered by subsurface inhomogeneities. This scattering allows the escape of a fraction of incident radiation that would otherwise be absorbed if the medium were uniform with depth. The higher reflection then results in a lower emissivity for a given dielectric constant through Kirchoff's law. This scenario presumes that the medium is sufficiently transparent to allow the scattering and ultimate escape of transmitted radiation, with a lower absorptivity likely to result in higher net loss and a resulting lower emissivity. This has been a favored explanation for the icy satellites of Saturn and Jupiter, for example, where cold, pure ices are known to have very low absorption and emissivities lower than 0.5 have been inferred in the microwave region (Ostro et al., 2006).

The general trend towards low brightness and higher radar reflectivity seen in Fig. 8 is consistent with volume scattering that varies from place to place over Titan's surface. With reference to the model calculations of Fig. 9, other effects that would produce signatures in Fig. 8 include rms slope variation with a fixed dielectric constant, which would produce a variable radar reflectivity with smaller variation in T_b (such as seen in the T7 points), and a surface with constant roughness but variable dielectric constant, which would produce a trace with smaller σ^0 and larger T_b variation (such as seen in the Ta points). Another important deviation from the simple model is the presence of roughness either on wavelength scales, or extreme roughness ($\gtrsim 30°$) on large scales, both of which would tend to produce higher emissivities for a given dielectric constant. All these effects must be considered to varying degrees in the interpretation of the SAR data and brightness temperature variations across Titan's surface.

4. SAR and radiometry correlation of selected features

Using the cumulative plot of Fig. 8, we outline the distribution and inverse correlation between radar reflection and brightness temperature of selected geologic features and terrains whose ranges of variability are listed in Table 4. We examine each swath in sequence from high latitude to low latitude as follow: Ta, T3, T8, T13, and T7. This sequence seems to reflect regional transitions observed on Titan's surface and it is best suited to describe them.

In Ta (Fig. 3), which is at the higher latitude (∼45 N) in this sequence, triangular-shaped features similar to alluvial fans east of the semicircular dome named Ganesa Macula and the large flow feature in the eastern end of the swath (Elachi et al., 2005b; Lopes et al., 2006) are good examples of the general inverse correlation shown in Fig. 8. The identified fan-shaped deposits (Paganelli et al., 2005) and flow features in Ta (Fig. 10) have distinct signatures in which the fan and associated deposit exhibit high radar reflectivity and very low radiometric brightness, while the flow feature to the east has lower radar reflectivity and higher radiometric brightness, on the order of 4 K, suggesting a possibly different genetic origin. A reduced radiometric brightness temperature and increased radar backscattering suggests that volume scattering could derive from near-surface structures or compositional and textural changes such as low absorbing-porous materials or heterogeneous materials such as alluvial fans (Paganelli et al., 2005). The flow feature has been interpreted as cryovolcanic in origin (Lopes et al., 2006) and its distinctive radiometric signature favors the interpretation as fluid flow perhaps cryovolcanic in origin (Fig. 10).

The Ganesa Macula terrain is perhaps unique as no similar features have been imaged so far, but it exhibits characteristics comparable to the intermediate terrain surrounding the fan-shaped deposits and flow features in the swath (Fig. 10). This suggests either similar composition such as water–ice and water–ammonia ice or similar surface roughness and textural characteristics at the radar wavelength scale. The Ta swath exhibits an overall reduced radar cross-section, ∼2 dB, when compared to the radar brightness of T3, T7, T8, and T13. Ta is at higher latitude (∼45°) compared to the other swaths, and thus exhibits in general widespread low radar reflective terrain that can justify the observed reduced radar cross-section.

In T3 at ∼15 N latitude (Fig. 4), two impact features, the 80-km impact crater named Sinlap and the ∼450-km Menrva impact basin (Stofan et al., 2006; Elachi et al., 2006), appear as some of the coldest regions thus far covered by SAR-radiometry. Another very prominent cold region is defined by the fans and alluvial bright deposits (Elachi et al., 2006) east of Menrva impact basin. Also apparent in T3 are the dune fields in the western and central portion of the swath, which show some of the radiometrically warmest regions imaged at this latitude.

The relationship of radar reflectivity and brightness temperature of cold features such as alluvial fans and plains, the rim of Menrva impact basin, Sinlap ejecta, and the hills region in T3 (Fig. 11) exhibit a clear inverse correlation. Here the degree of variability between the cold features and the surrounding terrains is in the order of 4–6 K, with 6 K found in the T3 fan-shaped features and associated alluvial deposits, one of the coldest areas observed. The high radar reflectivity and low brightness temperature in this region suggests heterogeneous materials common in alluvial fans, consistent with the presence of a mixture of higher dielectric constant and higher roughness.

The localized dunes covering terrains in T3 were the first to be imaged (Elachi et al., 2006), followed by the discovery of

Table 4
Summary of normalized σ^0 and brightness temperature T_b [K] for identified terrains and features

		Dunes	Mezzoramia embayment	Ganesa Macula terrain	Intermediate terrains	Shikoku Facula/ Guabonito	Fans/ alluvium	Flows	Hills/eroded edifices	Craters: Sinlap/ Menrva	Xanadu	Huygens landing site
Ta	σ^0			0.11–0.33	0.11–0.52		0.17–0.68	0.28–0.74				
	T_b			76.13–82.12	77.77–83.04		70.81–77.74	76.89–80.87				
T3	σ^0	0.14–0.65			0.23–1.18		0.83–1.44		0.45–1.62	0.88–1.73		
	T_b	80.94–84.79			76.78–82.04		67.12–74.48		73.30–76.98	67.55–75.26		
T7	σ^0		0.07–0.39									
	T_b		82.89–85.82									
T8	σ^0	0.05–0.36			0.16–0.98				0.31–1.13			0.42
	T_b	84.59–86.53			79.99–85.69				74.59–81.76			82.69
T13	σ^0	0.09–0.28				0.20–1.05					0.42–1.28	
	T_b	82.80–88.55				82.09– 88.16					64.71–84.16	
Summary	σ^0	0.05–0.65	0.07–0.39	0.11–0.33	0.11–1.18	0.20–1.05	0.17–1.44	0.28–0.74	0.31–1.62	0.88–1.73	0.42–1.28	0.42
	T_b	80.94–88.55	82.89–85.82	76.13–82.12	76.78–85.69	82.09–88.16	67.12–77.74	76.89–80.87	73.30–81.76	67.55–75.26	64.71–84.16	82.69

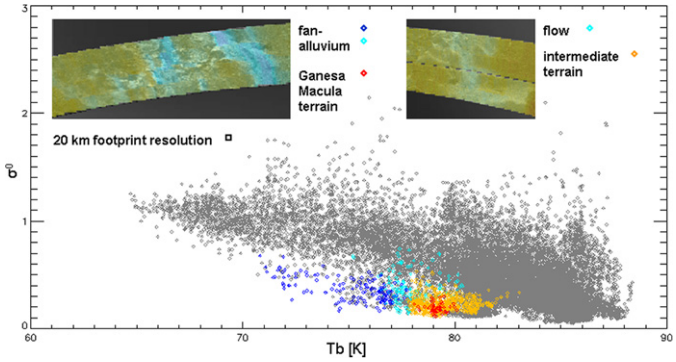

Fig. 10. Scatterplot of normalized radar cross section (σ^0) versus brightness temperature (T_b) of selected features in Ta: Ganesa Macula terrain; fan/alluvium; flow feature; intermediate terrain. The selected features are plotted on the cumulative scatterplot of σ^0 versus T_b for context and to allow correlation with other swaths and features. A surface with constant roughness but variable dielectric constant would produce a trace with smaller σ^0 and larger T_b variation as the one observable in the Ta Ganesa dome and surrounding terrains which may indicate a varying average dielectric constant.

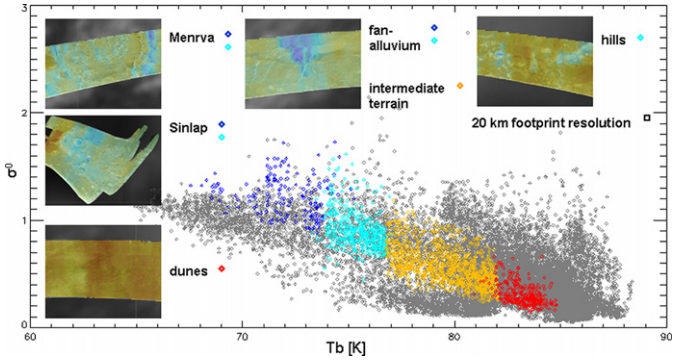

Fig. 11. Scatterplot of normalized radar cross section (σ^0) versus brightness temperature (T_b) of selected features in T3: Menrva basin and Sinlap crater; hills area; fan/alluvium; dunes area. The general trend towards low brightness and higher radar reflectivity seen in T3 in the Menrva and Sinlap terrains is consistent with a higher dielectric constant or with heterogeneous materials such as ice-rocks of variable lower dielectric constants including also solid hydrocarbons ($\varepsilon = 2.0$–2.4; Thompson and Squyers, 1990) and a size greater than the operational radar wavelength of 2.18 cm inducing volume scattering that varies from place to place over Titan's surface.

wider dune fields (e.g. T8 and T13) spread within 15° latitude of Titan's equatorial belt. The dunes area in the central portion of T3 (Fig. 11) is the warmest of such terrains observed in T3, and shows a 4–6 K contrast with the surrounding terrains.

The localized hills region, eroded high standing edifices such as the Menrva rim, or the ejecta blanket of Sinlap crater (Fig. 11), are cases in which reduced brightness temperature and increased radar reflection could be more likely ascribed to the effects of topography, surface roughness or dielectric constant variations (Paganelli et al., 2006a, 2006b). Here the degree of variability between the cold features and the surrounding terrains is 4–6 K in Sinlap, 6 K at the Menrva's east basin ring, and 4–5 K in the hills region. These features could expose deeper, denser and higher dielectric constant materials compared to the surrounding plains that could account for the reduced brightness temperature due to increased scattering. The Sinlap crater was seen during the T3 and Ta outbound passes (Elachi et

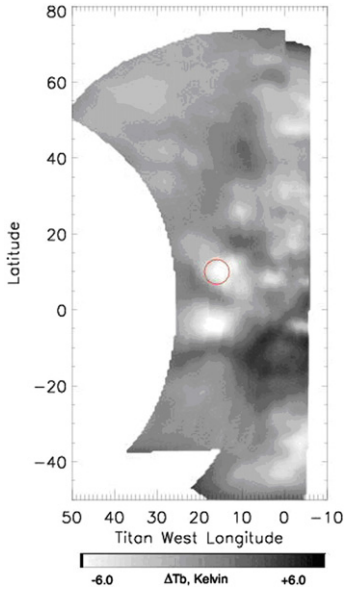

Fig. 12. A composite map of relative brightness temperature accompanying the scatterometry for the Ta and T3 outbound passes. Limb darkening has been accounted for in order to bring out brightness temperature contrast (inverted image). The red circle indicates a radiometrically cool feature surrounding the 80-km crater observed in the SAR and SAR-radiometry (from Elachi et al., 2006).

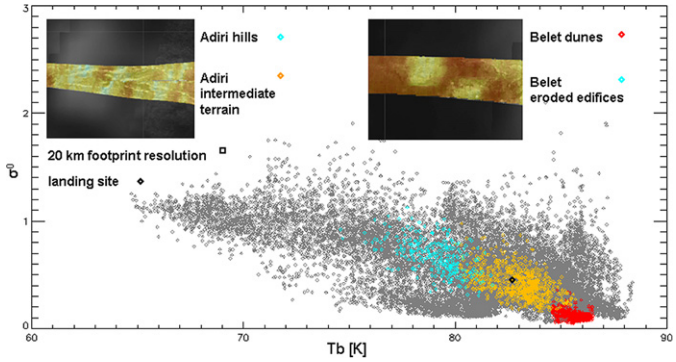

Fig. 13. Scatterplot of normalized radar cross section (σ^0) versus brightness temperature (T_b) of selected features in T8: Adiri hills and intermediate terrain; Belet dunes and Belet eroded edifices; the Huygens landing site. The low radar return and the high emissivity of the Belet dunes suggest a combination of smooth surfaces of homogeneous organic fine-textured materials with low dielectric constant (2.0–2.4 solid hydrocarbons).

al., 2006) using both low-resolution radiometry (Janssen et al., 2005b) and scatterometry (Wye et al., 2007). Allowing for the low resolution of the radiometer and scatterometer data (50–150 km), the identified cold feature coincides approximately with the extent of the ejecta blanket seen in the SAR and SAR-radiometry swaths (Figs. 4, 11). This feature was estimated to have approximately a 6 K contrast with the nearby terrain (Fig. 12), which is consistent with the SAR-radiometry results, and is one of the coldest spots yet observed by the radiometer. As suggested above, the reduced emissivity in the crater and ejecta blanket can be explained by an increase in dielectric constant, suggesting for example an increase in dielectric constant from 2 to 4.5, or a combination of higher dielectric constant and volume scattering. This could suggest the exposure of deeper materials with higher amount of water–ammonia ice ($\varepsilon = 4.5$) within the crater and the ejected material relative to the surrounding plains. The crater and blocky ejecta are features in which multiple-facet bounces of the radar signal are likely to produce a volume scattering component that can make a significant contribution to the overall radar reflectivity.

In T8, the first equatorial flyby (Fig. 6), more dune fields were imaged (Lorenz et al., 2006), hilly terrain or mountain chains (Lunine et al., 2007; Radebaugh et al., 2007), along with coverage of the Huygens landing site in the most eastern portion of the swath (Tomasko et al., 2005; Lunine et al., 2007). The radiometry in this swath shows a remarkable contrast between the vast areas covered by the dune fields and the eroded hills or high-standing edifices.

Hills and rough terrains present in the Adiri region (Figs. 6 and 13) exhibit high radar reflectivity and low brightness temperature characteristics similar to those observed for the T3 hills, the Menrva and Sinlap edifices. Here the emissivity is slightly lower, with the lowest values associated with some of the coldest spots at 76 K. Analogously to the T3 hills region, these features could expose deeper materials that could account for the reduced brightness temperature due to the presence of a higher dielectric constant relative to the surrounding plains.

In the Belet dunes area (Fig. 13) the brightness contrast between the warm dune fields and the surrounding terrains is ∼7 K, slightly higher compared to the 4–6 K observed in T3 warmest dunes area. In the Belet dunes as well as for the T3 dune areas the increased brightness temperature and reduced radar reflectivity suggests that low or no volume scattering is present and that the observed relationship could derive from smooth surfaces with homogeneous highly-absorbing and fine textured materials comprising the dunes. In this context, the increased brightness could be associated with a transition to a lower dielectric constant between cold and warm regions, suggesting the dune areas could be characterized by smooth surfaces of homogeneous organic fine-textured materials (i.e. 0.100–0.250 μ size particles) with low dielectric constant such as solid hydrocarbons ($\varepsilon = 2.0$–2.4) or clathrates ($\varepsilon = \sim 1.8$).

The Huygens landing site is located at 192.4° W and 10.2° S (Figs. 6 and 13) in an area of intermediate brightness terrain with $T_b = 82$ K and intermediate radar reflectivity $\sigma^0 = 0.4$, suggesting the presence of mixed terrain. From the mosaic of the DISR images (DISR mosaic covers a surface of ∼25 km^2) superimposed on the T8 SAR swath (Kirk et al., 2005; Lunine et al., 2007), it can be seen that the landing site is in an area with relatively low radar reflectivity with sporadic bright patches and dark-albedo linear features, visible in several of the highest-altitude DISR images, matching linear dunes in the SAR image.

In T13, the second equatorial flyby (Fig. 7), we have the highest contrast of brightness temperature observed so far due to the presence of the low reflective Shangri–La dunes region and the very high radar reflectivity characterizing the Xanadu region. The Xanadu region is characterized by the highest radar reflectivity and lowest brightness temperatures observed so far (Fig. 14). Clear evidence of topography (Kirk et al., 2005) and a very rough surface on large scales identify this region as unique.

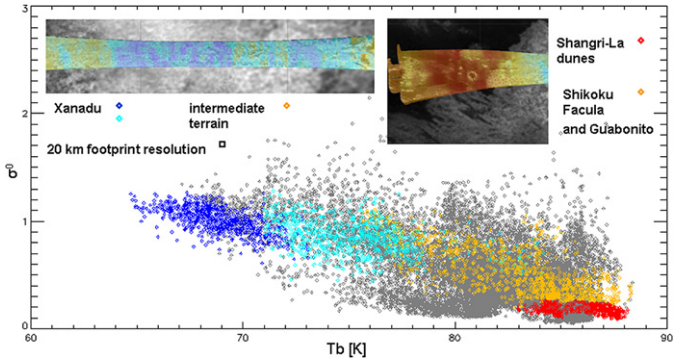

Fig. 14. Scatterplot of normalized radar cross section (σ^0) versus brightness temperature (T_b) of selected features in T13: Xanadu terrain; Shangri–La dunes; Shikoku Facula and Guabonito terrains. Xanadu terrain is the coldest region observed and can be associated with a low absorbing-porous material with a mixture of low (i.e. snow and fractured ice, $\varepsilon = 3.12$) and high dielectric constant (i.e. water–ammonia–ice, $\varepsilon = 4.5$). Similar behaviors suggest the presence of similar volume scattering in other areas where hills and rugged terrains are present as in part of Shikoku Facula and Guabonito.

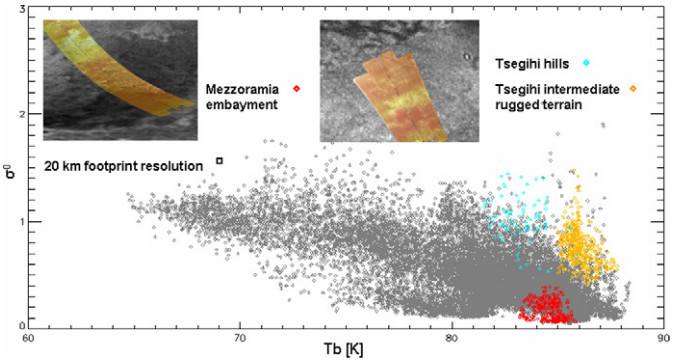

Fig. 15. Scatterplot of normalized radar cross section (σ^0) versus brightness temperature (T_b) of selected features in T7: Mezzoramia embayment; Tsegihi hills; Tsegihi intermediate rugged terrain. The Mezzoramia lacustrine area suggests a smooth surface of solid or liquid hydrocarbons ($\varepsilon = 1.6$–1.9) or plains of solid non-water–ice materials (solid organics and sludge with dielectric constant ~2.0) which are consistent with the observed high brightness temperatures and low radar reflectivity.

The low brightness temperature is a strong indication of significant volume scattering in this region. The corresponding high radar return is consistent with this interpretation. Emissivities <70% are suggestive of surfaces like those of the icy satellites (Ostro et al., 2006), and further work is suggested to quantify the similarity between these regions.

In contrast, the Shangri–La dune field in the western portion of the swath (Fig. 6), shows the highest brightness temperature detected in Titan's equatorial belt. The Shangri–La dune field, between Shikoku Facula and Guabonito (Fig. 14), shows the same type of terrain relationship observed in areas covered by dune fields in the T3 and T8 swaths (Figs. 11 and 13). In this context, the increased radiometric return could be associated with high emissivity due to a transition to a lower dielectric constant between cold and warm regions. Here the contrast between the dunes field and the adjacent Shikoku Facula and Guabonito terrains is in the order of 7 K, among the highest observed.

In T7 (Fig. 5), the only flyby thus far covering the southern hemisphere (~60 S) of Titan, a variety of terrain types are imaged that range from hills and plateau dissected by pervasive drainage patterns to a flood plain and a semicircular embayment (Lunine et al., 2007). Due to a solid-state recorder anomaly only half of the planned SAR pass was recovered. There is a higher degree of uncertainty in this swath due to unavailable calibration data for zero offset and gain correction; nevertheless, the accuracy of these brightness temperatures is +/−8 K. That said, the SAR-radiometry seems to retain the same inverse correlation observed so far.

This flyby offered a unique close look at the Mezzoramia region, one of the most interesting and intriguing areas covered so far. The Mezzoramia semicircular embayment shows a transition from bright to dark regions in the SAR swath, accompanied by an inverse correlation in the SAR-radiometry map. The Mezzoramia low radar reflectivity and high brightness temperature (Fig. 15) identify this terrain as similar to the dunes covered terrains observed in T3, T8 and T13.

At the Mezzoramia embayment the degree of variability between the warm embayment and the transition to surrounding terrains is about 3 K, lower than those observed for the dunes in T3, T8 and T13. This suggests the possibility that the low radar-reflective Mezzoramia embayed terrain might be a dry lake with infilling of solid organic material similar in composition and dielectric properties to the dunes, perhaps the reservoir of fine particulate material that is swept away and accumulated in the aeolian deposits mainly observed in the equatorial region of T8, T13 and T3. However, we cannot rule out the possibility of infilling of liquid hydrocarbons ($\varepsilon = 1.6$–1.9; Thompson and Squyers, 1990; Lorenz et al., 2003) in the Mezzoramia embayment. Although the Mezzoramia embayment shows a clear transition between the bright and dark terrains in SAR data, this is more subtle in the radiometry data (3 K), which could suggest that the margins of the embayment are made by the same material but is simply rougher on a scale of centimeters, or that deposits of rougher material (perhaps lacustrine) are present on the margins.

The Tsegihi area, in the northern portion of the swath, is also very interesting and characterized by bright hills surrounded by rugged terrains that have some of the highest radar reflectivity and highest brightness temperature observed for rough surface terrains (Fig. 15). Although the uncertainty in the calibration, the large excursion of radar reflectivity and minimal variation in brightness temperature observed especially for the Tsegihi intermediate rugged terrain (around 2 K), compare to the more spread distribution observable for the Tsegihi hills, suggests a possible slope effect associated with constant dielectric material, such as a mixture of solid hydrocarbons ($\varepsilon = 2.0$–2.4) with snow and fractured ice ($\varepsilon = 3.12$). The Tsegihi hills are cooler and could suggest the exposure of deeper materials with higher amount of water–ammonia ice ($\varepsilon = 4.5$) relative to the surrounding terrains.

5. Conclusions and future work

The comparison of Titan's radiometric brightness at high resolution with concurrent SAR reflectivity shows promise for

contributing to our understanding of the nature of Titan's surface. The inverse correlation in which terrains with high radar reflectivity are associated with radiometrically cold regions is generally consistent with varying degrees of volume scattering from one region to the next, an interpretation that is consistent with previous interpretations of radiometry at lower resolution (Janssen et al., 2005a; Elachi et al., 2006). The coldest regions can be associated with low absorbing-porous material with a mixture of low (i.e. snow and fractured ice, $\varepsilon = 3.12$) and high dielectric constant (i.e. water–ammonia–ice, $\varepsilon = 4.5$). Alternatively, they can also represent areas with heterogeneous materials such as ice-rocks, with variable dielectric constants including also solid hydrocarbons ($\varepsilon = 2.0$–2.4; Thompson and Squyers, 1990) and a size greater than the operational radar wavelength of 2.18 cm. The presence of volume scattering is most evident in the Xanadu region, which exhibits both the highest radar return and coldest brightness temperatures. Similar behavior suggests the presence of similar volume scattering in other areas where hills and craters are present (i.e., T3, T7, T8, and T13), and rugged terrains with channels and fan/flow features have been seen, such as in Ta, T3, and T7.

An inverse correlation has also been observed when analyzing terrains with lower radar reflectivity and high brightness temperature, radiometrically warm regions, which characterize the regions covered by aeolian dune fields (T3, T8, and T13) and lacustrine areas (Ta and T7). In the dune fields observed in T3, T8 and T13, the low radar return and the high emissivity suggest a combination of smooth surfaces of homogeneous organic fine-textured materials with low dielectric constant (2.0–2.4 solid hydrocarbons or clathrates $\varepsilon = \sim 1.8$) that comprise the dunes. In the lacustrine areas mainly present in patches in Ta and the extended Mezzoramia embayment in T7, smooth surfaces like ponds of solid or liquid hydrocarbons ($\varepsilon = 1.6$–1.9) or plains of solid non-water–ice materials (solid organics and sludge with dielectric constant ~ 2.0 or clathrates $\varepsilon = \sim 1.8$) are consistent with the observed high brightness temperatures and low radar reflectivity. We compiled a summary table (Table 4) listing the range of variability of radar reflectivity and brightness temperature based on the various features and terrains analyzed in this paper. This is a preliminary reference to which more features and terrains will be added as more flybys give us a more extensive coverage of Titan.

The potential of this approach will grow as more radiometry and SAR data are obtained. First, more of Titan will be seen at low resolution, allowing more of the radiometry obtained in SAR mode to be directly calibrated. Second, more high-resolution data will enable a detailed model of the sidelobe pattern to be determined. These will allow an improvement in absolute accuracy by a factor of two and enable correspondingly more precise interpretations. Differing signatures in the correlation between brightness temperature and radar reflectivity indicate that other effects than volume scattering such as dielectric constant, surface slope variations, and wavelength-scale roughness may be important in other regions. The above observations are summarized in the plot in Fig. 16 in which we outline features and terrains behavior in association to their physical properties. Modeling for these cases that accounts for both the radar backscatter and emissivity will aid in the interpretation. We are currently developing a quantitative model to explain the correlation between brightness variations and σ^0, which will be discussed in a future paper.

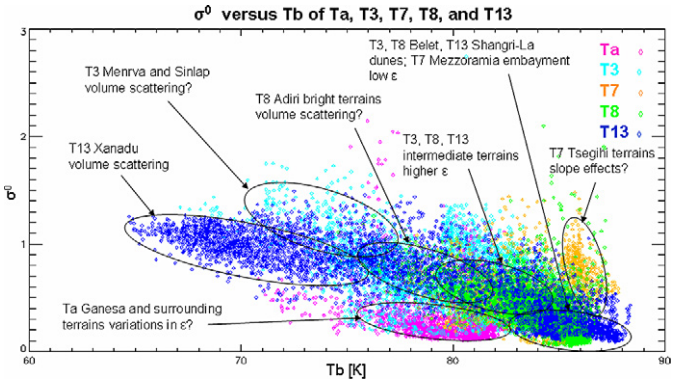

Fig. 16. Cumulative scatterplot of normalized radar cross section (σ^0) versus brightness temperature (T_b) of Ta, T3, T7, T8, and T13: outline features and terrains behavior in association to their physical properties.

Based on Titan's model behavior expected materials on the surface of Titan comprise solid hydrocarbons ($\varepsilon = 2.0$–2.4), clathrates ($\varepsilon = \sim 1.8$), water ice ($\varepsilon = 3.1$), water–ammonia ice ($\varepsilon = 4.5$), or combinations thereof. This context creates a very complex environment that we are just beginning to explore. Experimental laboratory work is needed to establish the microwave properties of these complex materials as well as their other physical properties.

Finally, correlations are apparent among the active and passive radar data and ISS and VIMS data that beg quantitative examination along the line explored here. A collaboration to include IR and optical imaging data in these comparisons offers the possibility of reaching a deeper understanding of the complex physical and chemical properties of Titan's surface that remain ambiguous in the present approach.

Acknowledgments

This work was conducted at the Jet Propulsion Laboratory, California Institute of Technology, under the National Research Council Resident Research Associateship NASA Postdoctoral Program. We also acknowledge those who designed, developed, and operate the Cassini/Huygens mission, which is a joint endeavor of NASA, the European Space Agency (ESA), and the Italian Space Agency (ASI) and is managed by JPL California Institute of Technology, under contract with NASA.

Appendix A. Status on radiometry calibration and sidelobe contributions

To summarize the calibration of the radiometer, we note that the measured quantity is the total power collected by the antenna, while the quantity of interest is the mean brightness temperature observed by the main beam. The total radiant power collected by the antenna is called the antenna temperature, and

may be written as

$$T_a(\Omega) = \int_{4\pi} T_b(\Omega') G(\Omega', \Omega)\, \mathrm{d}\Omega'. \quad (A.1)$$

where $T_b(\Omega')$ is brightness temperature in the direction of the solid angle element $\mathrm{d}\Omega'$ and $G(\Omega', \Omega)$ is the gain of the antenna in the same direction for an antenna pointed in the direction Ω. The gain pattern is typically normalized so that

$$\int_{4\pi} G(\Omega', \Omega)\, \mathrm{d}\Omega' = 1. \quad (A.2)$$

Equation (A.1) may be rewritten to show the effect of antenna gain outside the main beam (the sidelobes)

$$\begin{aligned} T_a(\Omega) = &\int_{\mathrm{mb}} T_a(\Omega) G(\Omega', \Omega)\, \mathrm{d}\Omega' \\ &+ \int_{\text{source-mb}} T_a(\Omega) G(\Omega', \Omega)\, \mathrm{d}\Omega' \\ &+ \int_{\text{cold sky}} T_a(\Omega) G(\Omega', \Omega)\, \mathrm{d}\Omega' \end{aligned} \quad (A.3)$$

where the integration over solid angle has been separated into three parts:

(1) integration over the main beam solid angle (mb),
(2) integration over the solid angle of the source exclusive of the main beam (source-mb),
(3) integration over the remainder of the sky.

If we renormalize the gain pattern so that only the contribution from the main beam is considered

$$\int_{\mathrm{mb}} G(\Omega', \Omega)\, \mathrm{d}\Omega' = 1 \quad (A.4)$$

then Eq. (A.3) can be rewritten as

$$T'_a(\Omega) = \bar{T}_b^{\mathrm{mb}}(\Omega) + \bar{T}_b^{\mathrm{sl}}(\Omega), \quad (A.5)$$

where $\bar{T}_b^{\mathrm{mb}}$ is the desired quantity, or the average brightness temperature in the footprint defined by the main beam. $\bar{T}_b^{\mathrm{sl}}$ is the net contribution from the sidelobes that fall onto both the extended source and empty space. Our calibration approach uses known signals to calibrate only the main beam contribution. In particular, we observed Titan from sufficient distance that its size was comparable to or less than that of the main beam, and Saturn from distances where the sidelobe contribution was readily accountable (i.e., $\leqslant 1\%$). The calibration used in this paper was obtained using an observation of Saturn by the radiometer in April, 2004 from a distance of approximately 20 Saturn radii, which was compared with observations of Saturn from the Very Large Array in New Mexico at 2.0 cm. A measured Saturn disk temperature of 141 K at 2.0 cm (Grossman, 1990; de Pater and Dickel, 1991; Molnar and Dunn, 1997) was used to calibrate beam 3. Distant observations of Titan were made periodically to ensure that the calibration is stable with time, and to give a corroborating calibration since Titan's disk temperature at 2.0 cm has also been measured from the VLA (Butler and Gurwell, 2004; Butler, private communication). The gains of beams 1, 2, 4, and 5 were adjusted to be consistent with that of beam 3 using integrations over their measured patterns.

The sidelobe contribution $\bar{T}_b^{\mathrm{sl}}$ depends on the apparent size of the extended source and its brightness; e.g., as the spacecraft moves closer to Titan its apparent disk fills the extended sidelobes and increases $\bar{T}_b^{\mathrm{sl}}$ correspondingly. To first order this contribution is a function of the range to Titan, small at distances far from Titan and growing to as much as 30% of the total antenna temperature at closest approach. In accounting for this unwanted contribution we note first that it is unlikely to significantly affect the small-scale brightness structure observed during a given SAR pass, for three reasons: (1) the contribution is the result of an integration of distributed sidelobe structure over an extended source, (2) whereas the main beam is formed by the coherent combination of radiation across the entire antenna, sidelobes are generally caused by local effects which produce perturbations on the pattern that are necessarily broader in angular extent than the main beam, and (3) during a SAR pass the pointing is generally fixed with respect to the Titan disk and the motion of the spacecraft is used to scan the swath. For the purposes of this paper we identified and approximately removed $\bar{T}_b^{\mathrm{sl}}$ for beam 3 by fitting the average measured SAR brightness temperatures to calibrated low-resolution maps of Titan where the sidelobe contribution was readily accountable. The sidelobe contributions from beams 1, 2, 4, and 5 were determined using an approximate range-dependent function determined from the beam 3 data and requiring the average brightness temperature along each beam trace to equal the average along beam 3.

References

Butler, B.J., Gurwell, M.A., 2004. Radio wavelength observations of Titan with the VLA. Bull. Am. Astron. Soc. 36. 6.04.

de Pater, I., Dickel, J.R., 1991. Multifrequency radio observations of Saturn at ring inclination angles between 5 and 26 degrees. Icarus 94, 474–492.

Elachi, C., Allison, M.D., Borgarelli, L., Encrenaz, P., Im, E., Janssen, M.A., Johnson, W.T.K., Kirk, R.L., Lorenz, R.D., Lunine, J.I., Muhleman, D.O., Ostro, S.J., Picardi, G., Posa, F., Rapley, C.G., Roth, L.E., Seu, R., Soderblom, L.A., Vetrella, S., Wall, S.D., Wood, C.A., Zebker, H.A., 2005a. RADAR: The Cassini Titan Radar Mapper. Space Sci. Rev. 117, 71–110.

Elachi, C., Wall, S., Allison, M., Anderson, Y., Boehmer, R., Callahan, P., Encrenaz, P., Flamini, E., Francescetti, G., Gim, Y., Hamilton, G., Hensley, S., Janssen, M., Johnson, W., Kelleher, K., Kirk, R., Lopes, R., Lorenz, R., Lunine, J., Muhleman, D., Ostro, S., Paganelli, F., Picardi, G., Posa, F., Roth, L., Seu, R., Shaffer, S., Soderblom, L., Stiles, B., Stofan, E., Vetrella, S., West, R., Wood, C., Wye, L., Zebker, H., 2005b. First views of the surface of Titan from the Cassini RADAR. Science 308, 970–974.

Elachi, C., Wall, S., Janssen, M., Stofan, E., Lopes, R., Kirk, R., Lorenz, R., Lunine, J., Paganelli, F., Soderblom, L., Wood, C., Wye, L., Zebker, H., Anderson, Y., Ostro, S., Allison, M., Boehmer, P., Callahan, P., Encrenaz, P., Flamini, E., Francescetti, G.Y., Gim, Y., Hamilton, G., Hensley, S., Johnson, W., Kelleher, K., Muhleman, D., Picardi, G., Posa, F., Roth, L., Seu, R., Shaffer, S., Stiles, B., Vetrella, S., West, R., 2006. Titan Radar Mapper observations from Cassini's T_3 flyby. Nature 441, 709–713.

Fulchignoni, M., Ferri, F., Angrilli, F., Ball, A.J., Bar-Nun, A., Barucci, M.A., Bianchini, G., Bettanini, C., Borucki, W., Colombatti, G., Coradini, M.,

Coustenis, A., Debei, S., Falkner, P., Fanti, G., Flamini, E., Gaborit, V., Hamelin, M., Grard, R., Harri, A.M., Hathi, B., Jernej, I., Leese, M.R., Lehto, A., López-Moreno, J.J., Mäkinen, T., McDonnell, J.A.M., McKay, C.P., Molina-Cuberos, G., Neubauer, F.M., Pirronello, V., Rodrigo, R., Saggin, B., Schwingenschuh, K., Seiff, A., Simões, F., Svedhem, H., Tokano, T., Towner, M.C., Trautner, R., Withers, P., Zarnecki, J.C., 2005. In situ measurements of the physical characteristics of Titan's environment. Nature 438, 785–791.

Greffet, J.J., Nieto-Vesperinas, M., 1998. Field theory for generalized bidirectional reflectivity: Derivation of Helmholtz's reciprocity principle and Kirchhoff's law. J. Opt. Soc. Am. A 15, 2735–2744.

Grossman, A.W., 1990. Microwave imaging of Saturn's deep atmosphere and rings. Ph.D. thesis, Caltech, 188 pp.

Hobbs, P.V., 1974. Ice Physics. Clarendon Press, Oxford.

Janssen, M.A., 1993. An introduction to the passive microwave remote sensing of atmospheres. In: Janssen, M. (Ed.), Atmospheric Remote Sensing by Microwave Radiometry. Wiley & Sons, New York, Chapter 1, pp. 1–35.

Janssen, M.A., Lorenz, R., Elachi, C., Anderson, Y.Z., Boehmer, R.A., Gim, Y., Johnson, W.T.K., Kelleher, K.D., Lopes, R.M., Roth, L.E., Wall, S.D., West, R.D., 2005a. First mapping of Titan with the Cassini RADAR radiometer. Bull. Am. Astron. Soc. 36. 1075.

Janssen, M.A., Paganelli, F., Kirk, R., Lorenz, R.D., Lopes, R.M., and the Cassini RADAR Team, 2005b. Titan's surface properties from the Cassini RADAR radiometer. Bull. Am. Astron. Soc. 37. 739.

Kirk, R.L., Archinal, B.A., Tomasko, M.G., Rizk, B., Soderblom, L.A., Cook, A.D., Howington-Kraus, E., Becker, T.L., Rosiek, M.R., and the DISR Science Team, 2005. Topographic mapping of the Huygens landing site on Titan. Bull. Am. Astron. Soc. 37. Abstract 46.08.

Lopes, R., Mitchell, K.L., Stofan, E.R., Lunine, J.I., Lorenz, R., Paganelli, F., Kirk, R.L., Wood, C.A., Wall, S.D., Robshaw, L.E., Fortes, A.D., Neish, C.D., Radebaugh, J., Reffet, E., Ostro, S.J., Elachi, C., Allison, M.D., Anderson, Y., Boehmer, R., Boubin, G., Callahan, P., Encrenaz, P., Flamini, E., Francescetti, G., Gim, Y., Hamilton, G., Hensley, S., Janssen, M.A., Johnson, W.T., Kelleher, K., Muhleman, D.O., Ori, G., Orosei, R., Picardi, G., Posa, F., Roth, L.E., Seu, R., Shaffer, S., Soderblom, L.A., Stiles, B., Vetrella, S., West, R.D., Wye, L., Zebker, H.A., 2006. Cryovolcanic features on Titan's surface as revealed by the Cassini Titan RADAR Mapper. Icarus 186, 395–412.

Lorenz, R.D., 1998. Preliminary measurements of the cryogenic dielectric properties of water–ammonia ices: Implications for radar observations of icy satellites. Icarus 136, 344–348.

Lorenz, R.D., Janssen, M.A., West, R.D., Biolluz, G., Encrenaz, P., Muhleman, D.O., 2003. Cassini RADAR: Prospects for Titan surface measurements with passive radiometry. Planet. Space Sci. 51, 353–364.

Lorenz, R.D., Wall, S., Radebaugh, J., Boubin, G., Reffet, E., Janssen, M., Stofan, E., Lopes, R., Kirk, R., Elachi, C., Lunine, J., Paganelli, F., Soderblom, L., Wood, C., Wye, L., Zebker, H., Anderson, Y., Ostro, S., Allison, M., Boehmer, R., Callahan, P., Encrenaz, P., Ori, G.G., Franceschetti, G., Gim, Y., Hamilton, G., Hensley, S., Johnson, W., Kelleher, K., Muhleman, D., Picardi, G., Posa, F., Roth, L., Seu, R., Shaffer, S., Stiles, B., Vetrella, S., Flamini, E., West, R., 2006. The sand seas of Titan: Cassini RADAR observations of longitudinal dunes. Science 312, 724–727.

Lunine, J.I., Elachi, C., Wall, S.D.M., Allison, D., Anderson, Y., Boehmer, R., Callahan, P., Encrenaz, P., Flamini, E., Franceschetti, G., Gim, Y., Hamilton, G., Hensley, S., Janssen, M.A., Johnson, W.T.K., Kelleher, K., Kirk, R.L., Lopes, R.M., Lorenz, R., Muhleman, D.O., Orosei, R.S., Ostro, J., Paganelli, F., Paillou, P., Picardi, G., Posa, F., Radebaugh, J., Roth, L.E., Seu, R., Shaffer, S., Soderblom, L.A., Stiles, B., Stofan, E.R., Vetrella, S., West, R., Wood, C.A., Wye, L., Zebker, H., Alberti, G., Karkoschka, E., Rizk, B., McFarlane, E., See, C., Kazeminejad, B., 2007. Titan's diverse landscapes as evidenced by Cassini RADAR's third and fourth looks at Titan. Icarus, submitted for publication.

Molnar, L.A., Dunn, D., 1997. Time variability of the microwave structure of Saturn's atmosphere. Bull. Am. Astron. Soc. 29. 996.

Ostro, S.J., West, R.D., Janssen, M.A., Lorenz, R.D., Zebker, H.A., Black, G.J., Lunine, J.I., Wye, L.C., Lopes, R.M., Wall, S.D., Elachi, C., Roth, L., Hensley, S., Kelleher, K., Hamilton, G.A., Gim, Y., Anderson, Y.Z., Boehmer, R.A., Johnson, W.T.K., and the Cassini RADAR Team, 2006. Cassini RADAR observations of Enceladus, Tethys, Dione, Rhea, Iapetus, Hyperion, and Phoebe. Icarus 183, 479–490.

Paganelli, F., Elachi, E., Lopes, R.M., West, R., Stiles, B., Janssen, M.A., Stofan, E., Wood, C.A., Lorenz, R.D., Lunine, J., Kirk, R.L., Roth, L., Wall, S.D., Soderblom, L., and the RADAR Team, 2005. Channels and fan-like features on Titan imaged by the Cassini RADAR. Lunar Planet. Sci. XXXVI. Abstract 2150.

Paganelli, F., Janssen, M.A., Lopes, R.M., Stofan, E., Stiles, B., West, R., Roth, L., Wall, S.D., Lorenz, R.D., Lunine, J., Kirk, R.L., Elachi, C., Soderblom, L., and the RADAR Team, 2006a. A look at Titan surface from the Cassini RADAR SAR and radiometry data. Lunar Planet. Sci. XXXVII. Abstract 1497.

Paganelli, F., Janssen, M.A., Lopes, R.M., Stofan, E., Wall, S.D., Lorenz, R.D., Lunine, J.I., Kirk, R.L., Elachi, C., and the Cassini RADAR Team, 2006b. Titan's surface from the Cassini RADAR SAR and radiometry data. EGU06-A-05155 (abstract).

Porco, C.C., Baker, E., Barbara, J., Beurle, K., Brahic, A., Burns, J.A., Charnoz, S., Cooper, N., Dawson, D.D., Del Genio, A.D., Denk, T., Dones, L., Dyudina, U., Evans, M.W., Fussner, S., Giese, B., Grazier, K., Helfenstein, P., Ingersoll, A.P., Jacobson, R.A., Johnson, T.V., McEwen, A., Murray, C.D., Neukum, G., Owen, W.M., Perry, J., Roatsch, T., Spitale, J., Squyres, S., Thomas, P., Tiscareno, M., Turtle, E.P., Vasavada, A.R., Veverka, J., Wagner, R., West, R., 2005. Imaging of Titan from the Cassini Spacecraft. Nature 434, 159–168.

Radebaugh, J., Lorenz, R., Kirk, R., Lunine, J., and the Cassini RADAR Team, 2007. Mountains on Titan observed by Cassini RADAR. Icarus, in press.

Smith, P.H., Lemmon, M.T., Lorenz, R.D., Sromovsky, L.A., Caldwell, J., Allison, M.D., 1996. Titan's surface, revealed by HST imaging. Icarus 119, 336–349.

Stiles, B.W. Gim, Y., Hamilton, G., Hensley, S., Johnson, W.T.K., Shimada, J., West, R.D., Callahan, P., 2006. Ground processing of Cassini RADAR imagery of Titan. Proc. IEEE, submitted for publication.

Stofan, E., Lunine, J.I., Lopes, R., Paganelli, F., Lorenz, R., Wood, C., Kirk, R., Wall, S., Elachi, C., Allison, M.D., Anderson, Y., Boehmer, R., Boubin, G., Callahan, P., Encrenaz, P., Flamini, E., Francescetti, G., Gim, Y., Hamilton, G., Hensley, S., Janssen, M.A., Johnson, W.T., Kelleher, K., Muhleman, D.O., Ori, G., Orosei, R., Picardi, G., Posa, F., Roth, L.E., Seu, R., Shaffer, S., Soderblom, L.A., Stiles, B., Vetrella, S., West, R.D., Wye, L., Zebker, H.A., 2006. Mapping of Titan: Results from the first two radar passes. Icarus 185, 443–456.

Thompson, W.R., Squyers, S.W., 1990. Titan and other icy satellites: Dielectric properties of constituent materials and implications for radar sounding. Icarus 86, 336–354.

Tobie, G., Lunine, I.L., Sotin, C., 2006. Episodic outgassing as the origin of atmospheric methane on Titan. Nature 440, 61–64.

Tomasko, M., Archinal, B., Becker, T., Bézard, B., Bushroe, M., Combes, M., Cook, D., Coustenis, A., de Bergh, C., Dafoe, L., Doose, L., Douté, S., Eibl, A., Engel, S., Gliem, F., Grieger, B., Holso, K., Howington-Kraus, E., Karkoschka, E., Keller, H., Kirk, R., Kramm, R., Küppers, M., Lanagan, P., Lellouch, E., Lemmon, M., Lunine, J., McFarlane, E., Moores, J., Prout, M., Rizk, B., Rosiek, M., Rueffer, P., Schröder, S., Schmitt, B., See, C., Smith, P., Soderblom, L., Thomas, N., West, R., 2005. Rain, winds, and haze during the Huygens probe descent to Titan's surface. Nature 438, 765–778.

Ulaby, F.T., Moore, R.K., Fung, A.K., 1981. Microwave Remote Sensing: Active and Passive, Microwave Remote Sensing Fundamentals and Radiometry, vol. 1. Addison–Wesley, Reading, MA. 456 pp.

White, T.L., Cogdell, J.R., 1973. Lunar polarization studies at 3.1 mm wavelength. Moon 6, 235–249.

Wye, L.C., Zebker, H.A., Ostro, S.J., West, R.D., Gim, Y., Lorenz, R.D., and the Cassini RADAR Team, 2007. Electrical properties of Titan's surface from Cassini RADAR scatterometer measurements. Icarus 188, 367–385.